AN A-POSTERIORI ERROR ESTIMATOR FOR THE STABLE GENERALIZED/EXTENDED FINITE ELEMENT METHOD

Rafael Marques Lins
Sergio Persival B. Proença

mlins@sc.usp.br

persival@sc.usp.br

Department of Structural Engineering (SET), São Carlos School of Engineering (EESC), University of São Paulo (USP)

Avenida Trabalhador Sãocarlense, 400, 13566-590, São Carlos, SP, Brazil

Carlos Armando Duarte

caduarte@illinois.edu

Newmark Laboratory, Department of Civil and Environmental Engineering, University of Illinois at Urbana-Champaign

205 North Mathews Avenue, Urbana, IL 61801, USA

Abstract. *This study investigates the performance of a recovery-based a-posteriori error estimator in the framework of the Stable Generalized FEM (SGFEM). Different types of enrichment functions can be considered. When applied to linear Fracture Mechanics problems, this estimator is based on a splitting of the recovered stress field into two distinct parts: singular and smooth. The singular part is computed with the help of asymptotic expansions of the stress field nearby the crack tip, whereas the recovered smooth one is calculated from a combination between the Superconvergent Patch Recovery (SPR) and Singular Value Decomposition (SVD) techniques. Two numerical examples are selected to assess the robustness of the error estimator considering polynomial and special enrichment functions in two-dimensional analysis. Therefore, relevant aspects such as effectivity indexes, error distribution and convergence rates are used for assessing the error estimator. The main conclusion of this study is that the error estimator hereby developed can provide accurate results for both the GFEM and SGFEM. In particular, this feature can be used to verify the efficacy of the SGFEM even in problems without analytical solutions.*

Keywords: *Error estimation, Generalized FEM, Effectivity index, Fracture*

1 INTRODUCTION

In recent years, the Generalized FEM or Extended FEM (GFEM/XFEM), (Duarte et al., 2000; Strouboulis et al., 2001; Belytschko and Black, 1999; Moës at al., 1999), have been successfully applied to linear fracture mechanics problems due to their special features providing accurate solutions. Nevertheless, both methods may face hurdles in some problems due to the flexibility provided by the selective nodal enrichment with arbitrary functions. For example, the so-called blending elements, i.e., elements presenting nodes with different levels or types of enrichment attached, may affect the numerical accuracy locally, hence reducing the convergence rates. Moreover, the ill-conditioning of the stiffness matrix introduced by enrichment functions may lead to numerical solution polluted by round-off errors. More recently, researchers have sought to address these shortcomings by developing modified versions of the GFEM/XFEM, such as, the Corrected XFEM (Fries, 2008) and the Stable GFEM (SGFEM) (Babuŝka and Banerjee, 2012).

Despite the benefits demonstrated recently by the improved versions of the GFEM/XFEM, as is the case of the SGFEM, more investigation into the discretization errors associated to these methods is required. In particular, a posteriori error estimators, used to estimate the error when the exact solution is not available, are not common for the SGFEM. For this reason, this theme is discussed in Lins et al. (2015) and with more details in Lins (2015).This last work presents two a posteriori error estimators, which can be used with the GFEM and its improved versions mentioned above. This paper is focused on the GFEM and SGFEM and aims to show its benefits, specially in the SGFEM context.

Some previous research have already investigated the performance of the error estimators in the GFEM/XFEM context. Error estimators are often employed in adaptive methods aiming to reduce the error until a given tolerance with an optimized number of elements. For instance, Bordas et al. (2008) propose an error estimator based on the difference between an enhanced strain field, computed by extended moving least squares (XMLS), and the XFEM strain field. In this technique the branch functions are included as shape functions in the XMLS. More recently, this same error estimator was used in two distinct adaptive strategies by Jin et al. (2017) in the framework of the cracks treated by XFEM.

On the other hand, Ródenas et al. (2008) devise a technique called SPR_{XFEM}, where the key idea is to split the stress field into a smooth and a singular part. The smooth field is defined applying the superconvergent patch recovery (SPR), proposed by Zienkiewicz and Zhu (1992a, 1992b). The singular field, in turn, is defined by means of branch functions from Fracture Mechanics. Moreover, the stress intensity factors (SIFs) are calculated by the interaction integral (Shih and Asaro, 1988; Yau et al., 1980). The splitting technique is used only in a circular region at the vicinity of the crack tip. Prange et al. (2012) developed a new recovery procedure based on the Zienkiewicz and Zhu error estimator (Zienkiewicz and Zhu, 1987). The recovered stress field is calculated by means of a least squares fit.

In this paper, a new error estimator is proposed for the GFEM and SGFEM based on the estimator presented in Ródenas et al. (2008). The proposed estimator combines two techniques for computing the smooth part of the recovered stress field: the SPR and the Singular Value Decomposition (SVD) (Quarteroni et al., 2000). The singular part is computed with the help of the J integral (Rice, 1968). As the effectiveness of Ródena’s estimator was already demonstrated in Ródenas et al. (2008) in the XFEM framework, its extension to the SGFEM solutions also enables the evaluation of its effectiveness. The investigation is conducted comparing different features of the error estimator such as: effectivity index, rate of convergence and accuracy of recovered stresses. Different enrichment strategies and boundary conditions are hereby tested to provide a more comprehensive investigation. The effectiveness of the error estimator in the SGFEM framework is confirmed by the numerical results.

The rest of this paper is organized in the following way. In Sect. 2, the GFEM and the SGFEM are concisely described emphasizing the differences between them. In Sect. 3, the error estimator proposed hereby is detailed. In Sect. 4, the numerical results obtained using the error estimator considering two representative problems are shown. Finally, in Sect. 5, the most important findings and conclusions are summarized.

2 A BRIEF REVIEW OF GFEM/XFEM AND SGFEM

2.1 The GFEM/XFEM

The main difference between the standard FEM and the GFEM/XFEM is in the definition of the shape functions. In GFEM/XFEM, the shape functions ($\phi_{\alpha i}$) are defined locally in a domain ω_α called cloud or patch (set of elements that have a common vertex node). Inside of each cloud, the shape functions are constructed by the product between the so-called enrichment functions ($L_{\alpha i}$) and the linear partition of unity (PoU) functions belonging to the elements in the cloud and attached to the vertex α(φ_α). Therefore,

$$\phi_{\alpha i} = \varphi_\alpha L_{\alpha i} \tag{1}$$

where α identifies the nodal cloud and i = 1, …, nl, and nl is the total number of enrichment functions adopted for each cloud.

Figure 1 illustrates the construction of a GFEM/XFEM shape function in a two-dimensional domain.

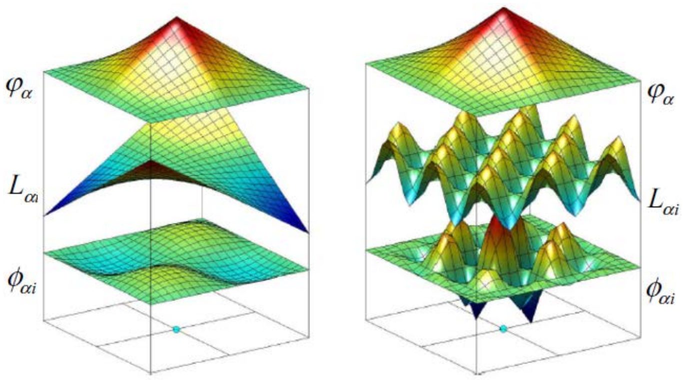

Figure 1. Representation of a GFEM/XFEM shape function. Here the FEM shape function, φ_α, is the function at the top and the enrichment function, $L_{\alpha i}$, is the function in the middle. The picture on the left depicts a polynomial enrichment function and the picture on the right depicts a non-polynomial enrichment function. The GFEM/XFEM shape function, $\phi_{\alpha i}$, is the resulting shape function shown at the bottom. This figure is adapted from Figure 1 of Kim el al. (2009).

Considering the unity as the first component of the set of enrichment functions, the global approximation space for the GFEM/XFEM can be split in a conventional FEM part and an enrichment part. Therefore, restricting only to 2-D problems, the GFEM/XFEM approximation for each component of the displacement field is given by the following relations:

$$\hat{u} = \sum_{\alpha=1}^{n} \varphi_\alpha u_\alpha + \sum_{\alpha=1}^{n} \varphi_\alpha \left(\sum_{i=2}^{nl} L_{\alpha i} b_{\alpha i} \right) \tag{2}$$

$$\hat{v} = \sum_{\alpha=1}^{n} \varphi_\alpha v_\alpha + \sum_{\alpha=1}^{n} \varphi_\alpha \left(\sum_{i=2}^{nl} L_{\alpha i} c_{\alpha i} \right) \tag{3}$$

where n is the number of nodal clouds, u_α and v_α are parameters associated with usual degrees of freedom of finite elements, $b_{\alpha i}$ and $c_{\alpha i}$ are additional nodal parameters introduced by enrichment. Clearly, the PoU matches the local enrichment approximations.

The enrichment functions aim to improve the quality of local approximation and can present special features or even be defined from previous knowledge of the solution. For instance, the so called branch functions are adopted to better represent the singular stress behavior at the crack tip. The branch functions, introduced in Oden and Duarte (1997) (these functions are hereafter denoted as OD), are hereby considered and represented as follows:

$$\begin{aligned} L_{OD-\bar{x}} &= \left\{ \sqrt{r}\left[\left(\kappa - \frac{1}{2}\right)\cos\frac{\theta}{2} - \frac{1}{2}\cos\frac{3\theta}{2} \right], \sqrt{r}\left[\left(\kappa + \frac{3}{2}\right)\sin\frac{\theta}{2} + \frac{1}{2}\sin\frac{3\theta}{2} \right] \right\} \\ L_{OD-\bar{y}} &= \left\{ \sqrt{r}\left[\left(\kappa + \frac{1}{2}\right)\sin\frac{\theta}{2} - \frac{1}{2}\sin\frac{3\theta}{2} \right], \sqrt{r}\left[\left(\kappa - \frac{3}{2}\right)\cos\frac{\theta}{2} + \frac{1}{2}\cos\frac{3\theta}{2} \right] \right\} \end{aligned} \tag{4}$$

where r and θ are polar coordinates attached to the crack tip (see Fig. 2), $-\pi < \theta < \pi$, κ is a material constant (3-4υ), and υ is the Poisson ratio. The $L_{OD-\bar{x}}$ branch functions are used for enrichment of the approximation along the local $\bar{x}$ direction and the $L_{OD-\bar{y}}$ branch functions are used for enrichment along the local $\bar{y}$ direction. Therefore, the OD branch functions introduce four additional DOFs per node.

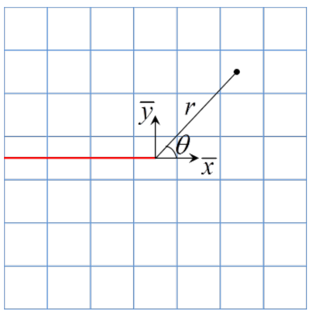

Figure 2. Description of the coordinate systems attached to crack tip

Another example of enrichment function is Heaviside function. This function is applied to capture displacement discontinuities caused by the existence of a crack. The Heaviside function used as enrichment is given by

$$H = \begin{cases} 1 & if\ \bar{y} \geq 0 \\ 0 & if\ \bar{y} < 0 \end{cases} \tag{5}$$

Unfortunately, the benefits due to the presence of enrichments in the GFEM/XFEM may be followed by some drawbacks such as: numerical integration difficulties, presence of blending elements and ill-conditioning of the system of equations. In the next section, the SGFEM is discussed which aims at addressing, in particular, the last issue mentioned.

2.2 The SGFEM

Due to the simplicity of its formulation and effective numerical results shown, the SGFEM, a modified version of GFEM/XFEM initially presented in Babuška and Banerjee (2012), has proved to be very attractive. Essentially, the basic difference between GFEM/XFEM and SGFEM is characterized by a modification of the enrichment functions. More precisely, in the SGFEM, the modified enrichment functions attached to a cloud are defined by the difference between the original enrichment function ($L_{\alpha i}$) and its piecewise linear or bilinear finite element interpolant function (I_{ω_α}). In other words,

$$L_{\alpha i}^{\text{mod}} = L_{\alpha i} - I_{\omega_\alpha}\left(L_{\alpha i}\right) \tag{6}$$

The interpolant function can be written as:

$$I_{\omega_\alpha} = \sum_{\alpha=1}^{ne} \varphi_\alpha L_{\alpha i}\left(x_\alpha, y_\alpha\right) \tag{7}$$

where (x_j, y_j) are the coordinates of node j of the element in question and ne refers to the number of element nodes.

The same procedure for constructing the GFEM/XFEM shape functions is used to define the SGFEM shape functions ($\phi_{\alpha i}^{\text{mod}}$). Hence,

$$\phi_{\alpha i}^{\text{mod}} = \varphi_\alpha L_{\alpha i}^{\text{mod}} \tag{8}$$

The interpolant function and the resulting shape function considered in SGFEM are highlighted in Figure 3.

It is important to note that to ensure accurate results of 2-D problems when using Heaviside functions in the SGFEM, the main requirement is the use of the linear Heaviside enrichment functions. The reasons for this requirement are discussed in detail in Gupta et al. (2013). Therefore, the linear Heaviside is also considered in this paper, as indicated below:

$$H_L = \left\{ H,\ H\frac{\left(x - x_\alpha\right)}{h_\alpha},\ H\frac{\left(y - y_\alpha\right)}{h_\alpha} \right\} \tag{9}$$

where H is defined in Eq. (5), x and y are global coordinates and h_α is a scaling factor given by the diameter of the largest element sharing node α.

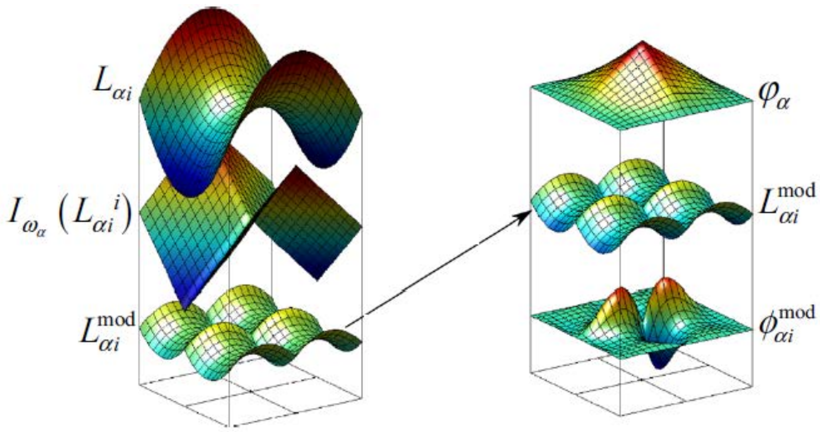

Figure 3. Construction of an enrichment function and a shape function used in SGFEM. The illustration on the left features the original enrichment function, $L_{\alpha i}$, at the top, the piecewise linear finite element interpolant of which is in the middle, $I_{\omega_\alpha}\left(L_{\alpha i}\right)$, and the modified SGFEM enrichment function, $L_{\alpha i}^{\mathrm{mod}}$, is shown at the bottom. The picture on the right depicts the construction of a SGFEM shape function, $\phi_{\alpha i}^{\mathrm{mod}}$. This figure is adapted from Figure 2 of Gupta et al. (2013).

3 THE ERROR ESTIMATOR

As already stated, the error estimator hereby proposed is based on some ideas originally presented in Ródenas et al. (2008). The keypoint is the splitting of the recovered stress field into two fields: a singular field $\boldsymbol{\sigma}_{\mathrm{sing}}^{*}$ and a smooth field $\boldsymbol{\sigma}_{\mathrm{smo}}^{*}$. This decomposition is applied only near the crack tip, since the singular field becomes negligible away from the crack tip.

In the first part of this section, the computation of each part defining the recovered stresses is described. Afterwards, an explanation is given on how the PoU can be used for joining the two fields aiming to build a global recovered approximation. In the last part, some concepts related to the assessment of the error are presented.

3.1 The singular field

As well-known, the stress field in the vicinity of the crack tip can be expressed through the first term of the Mode I and II asymptotic expansions (Szabó and Babuška, 1991). Hence,

$$\begin{Bmatrix} \sigma_{\mathrm{sing},xx} \\ \sigma_{\mathrm{sing},yy} \\ \tau_{\mathrm{sing},xy} \end{Bmatrix} = \frac{K_I}{\sqrt{2\pi r}} \cos\frac{\theta}{2} \begin{pmatrix} 1-\sin\frac{\theta}{2}\sin\frac{3\theta}{2} \\ 1+\sin\frac{\theta}{2}\sin\frac{3\theta}{2} \\ \sin\frac{\theta}{2}\cos\frac{3\theta}{2} \end{pmatrix} + \frac{K_{II}}{\sqrt{2\pi r}} \begin{pmatrix} -\sin\frac{\theta}{2}\left[2+\cos\frac{\theta}{2}\cos\frac{3\theta}{2}\right] \\ \sin\frac{\theta}{2}\cos\frac{\theta}{2}\cos\frac{3\theta}{2} \\ \cos\frac{\theta}{2}\left[1-\sin\frac{\theta}{2}\sin\frac{3\theta}{2}\right] \end{pmatrix} \tag{10}$$

Following Ródenas et al. (2008), Eq. (10) is adopted in this work to represent the recovered singular field $\boldsymbol{\sigma}_{\mathrm{sing}}^{*}$. This assumption is reasonable since $\boldsymbol{\sigma}_{\mathrm{sing}}^{*}$ can be estimated by means of approximate stress intensity factors K_I and K_{II}, computed using $\hat{\boldsymbol{\sigma}}$ (provided by GFEM or SGFEM solutions) in a post-processing. The J integral is hereby chosen to determine the SFI's, noting that when mixed mode of opening is considered, a decomposition of the J integral proposed by Ishikawa et al. (1980) is adopted.

3.2 The smooth field

Regarding the recovered smooth stress field $\boldsymbol{\sigma}^*_{\text{smo}}$, it is computed using the smooth part of the approximate stress field $\hat{\boldsymbol{\sigma}}$. However, as the enrichments include branch functions, the approximate field $\hat{\boldsymbol{\sigma}}$ given by GFEM/XFEM or SGFEM gathers two distinct parts: a singular part $\hat{\boldsymbol{\sigma}}_{\text{sing}}$ and a smooth part $\hat{\boldsymbol{\sigma}}_{\text{smo}}$. Therefore, its smooth part can be written as

$$\hat{\boldsymbol{\sigma}}_{\text{smo}} = \hat{\boldsymbol{\sigma}} - \hat{\boldsymbol{\sigma}}_{\text{sing}} \tag{11}$$

A key assumption in Eq. (11) is to replace $\hat{\boldsymbol{\sigma}}_{\text{sing}}$ by $\boldsymbol{\sigma}^*_{\text{sing}}$ obtained from Eq. (10). This assumption essentially stems from the consideration that the enrichment by branch functions already provides a good approximation to the singular field near the crack tip.

Once $\hat{\boldsymbol{\sigma}}_{\text{smo}}$ is defined, the SPR and SVD techniques briefly detailed below are then combined to calculate $\boldsymbol{\sigma}^*_{\text{smo}}$.

Superconvergent patch recovery (SPR)

In the SPR technique, the recovered stress field is described by a polynomial of the same degree as the displacement approximation field. The polynomial parameters are computed by means of a least squares fitting of the solutions for the stress field at the superconvergent points in each cloud. Once polynomial approximations of the recovered stresses are calculated in each cloud, nodal values at the cloud vertices are obtained by replacing the coordinates of the vertex node in the respective polynomial approximations. As a final step, the global recovered stress field is determined by pasting together the recovered nodal stress using the PoU displacement functions.

Singular value decomposition (SVD)

Aiming to better contextualize the role of the SVD, it is appropriate to summarize the problem under discussion. Essentially, a smooth polynomial approximation $\sigma^*_{p,i}$ should be identified from stress values $\hat{\boldsymbol{\sigma}}_i$ at superconvergent points defined in each cloud. This approximation can be written as

$$\sigma^*_{p,i} = \sum_{j=1}^{m} P_j\left(x, y\right) a_{j,i} \tag{12}$$

where $P_j\left(x, y\right)$ are the polynomial terms and $a_{j,i}$ is the set of unknown coefficients to be determined. For example, considering a bilinear polynomial approximation for cloud *i*, then: $\mathbf{P}\left(x, y\right) = \left\{1, x, y, xy\right\}$ and $\mathbf{a}_i = \left\{a_{1,i}, a_{2,i}, a_{3,i}, a_{4,i}\right\}^T$. Furthermore, m is the number of coefficients in the approximating polynomial.

Proceedings of the XXXVIII Iberian Latin-American Congress on Computational Methods in Engineering
P.O. Faria, R.H. Lopez, L.F.F. Miguel, W.J.S. Gomes, M. Noronha (Editores), ABMEC, Florianópolis, SC, Brazil, November 5-8, 2017.

In order to determine the coefficients vector $\mathbf{a}_i$ for each cloud, the following linear system is constructed considering s superconvergent points:

$$\mathbf{A}\mathbf{a}_i = \hat{\boldsymbol{\sigma}}_i \tag{13}$$

where

$$\mathbf{A} = \begin{bmatrix} P_1(x_1, y_1) & P_2(x_1, y_1) & \cdots & P_m(x_1, y_1) \\ P_1(x_2, y_2) & P_2(x_2, x_2) & \cdots & P_m(x_2, x_2) \\ \vdots & \vdots & \ddots & \vdots \\ P_1(x_s, y_s) & P_2(x_s, y_s) & \cdots & P_m(x_s, y_s) \end{bmatrix} \text{ and } \hat{\boldsymbol{\sigma}}_i = \begin{Bmatrix} \hat{\sigma}_{i,1}(x_1, y_1) \\ \hat{\sigma}_{i,2}(x_2, y_2) \\ \vdots \\ \hat{\sigma}_{i,s}(x_s, y_s) \end{Bmatrix} \tag{14}$$

Essentially, the system imposes the equality among the values $\sigma^*_{p,i}(x_k, y_k)$ provided by the polynomial approximation and the values $\hat{\boldsymbol{\sigma}}_i(x_k, y_k)$ at superconvergent points.

If matrix **A** is square, the resulting polynomial performs an interpolation of the prescribed values at the superconvergent points. However, when the number of the superconvergent points is greater than the number of coefficients, matrix **A** is rectangular. Consequently, the goal in this case is to find a solution representing the best fitting to the values at superconvergent points. Indeed, the motivation for applying the SVD derives from its known efficiency to perform such a fitting. Moreover, the proposed approach provided by the SVD technique can be considered more straightforward than the original SPR, since it does not require any functional. In addition the computational cost is low since the procedure involves only local (cloud) computations, as opposed to, e.g., a global projection as performed in Schweitzer (2013).

It is important to note that in accordance with the SVD procedure, the determination of coefficients $\mathbf{a}_i$ is guaranteed if, and only if, the number of optimal sampling points is greater than or equal to the number of coefficients. However, such a condition may not be satisfied in the clouds located close to the boundary due to the insufficient number of superconvergent points. For the sake of conciseness, the procedure for overcoming this hurdle is not detailed here. Such an aspect as well as some others features regarding the SVD are addressed in Lins (2015).

3.3 The global recovered stress field combining the singular and smooth fields

In general, a point inside the domain, covered by different clouds, is overlapped by different recovered stress fields. The procedure hereby adopted for pasting together the recovered stress fields in order to define a globally continuous field, explores the PoU as done in relations (2) and (3). However, the strategy for such construction is an element by element based approach, instead of a cloud by cloud approach. Therefore, the recovered stress for each stress component i can be written as:

$$\sigma^*_\alpha = \sum_{\alpha=1}^{ne} \varphi_\alpha \left(\boldsymbol{\sigma}^*_{\text{sing},\alpha} + \boldsymbol{\sigma}^*_{\text{smo},\alpha} \right) \tag{15}$$

where *ne* is the number of nodes of the element. It must be emphasized that in $\boldsymbol{\sigma}^{*}_{\mathrm{sing},\alpha}$ the index α is referred to the nodes of the element enriched with branch or Heaviside functions. This feature enables us to represent the recovered stresses close to the crack tip accurately, as well as to capture the discontinuity of the solution introduced by the crack.

Figure 4 aims to illustrate the use of Eq. (15). The purpose in this case is to compute the component σ^{*}_{xx} of the recovered stress field at points A and B. According to Eq. (15), the component σ^{*}_{xx} in these points is given by:

$$
\begin{aligned}
\sigma^{*}_{xx}(x_A, y_A) &= \sum_{\alpha=1}^{4} \varphi_\alpha(\xi_A,\eta_A)\,\sigma^{*}_{\mathrm{smo},xx(\alpha)}(x_A,y_A) + \sum_{\alpha=1}^{4} \varphi_\alpha(\xi_A,\eta_A)\,\sigma^{*}_{\mathrm{sing},xx}(x_A,y_A) \\
\sigma^{*}_{xx}(x_B, y_B) &= \sum_{\alpha=1}^{4} \varphi_\alpha(\xi_B,\eta_B)\,\sigma^{*}_{\mathrm{smo},xx(\alpha)}(x_B,y_B)
\end{aligned}
\tag{16}
$$

where α refers to the element node. Note that in Eq. (16), the smooth fields are computed by Eq. (12), whereas the singular fields are computed by Equation (10).

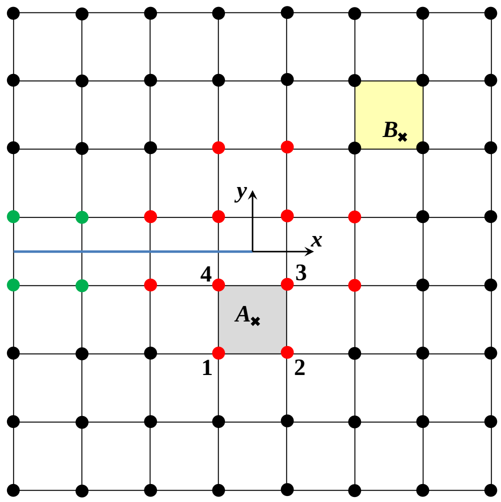

Figure 4. Arbitrary mesh used to illustrate the use of Eq. (15). The crack is represented by the blue line. The red nodes are enriched with the branch functions. The green nodes are enriched with the Heaviside function.

3.4 Error assessment

Due to the enrichment functions when a certain problem is analyzed by GFEM/XFEM or SGFEM, the discretization error may decrease significantly in comparison to the standard FEM. However, some error still remains. The error in energy can be computed exactly if there is an analytical solution to the problem. Hence, in each element the energy norm of the exact error is defined as

$$
\|e\|_{\Omega_e} = \left[\int_{\Omega_e} (\boldsymbol{\sigma} - \hat{\boldsymbol{\sigma}})^T \, \mathbf{D}^{-1} (\boldsymbol{\sigma} - \hat{\boldsymbol{\sigma}})\, d\Omega_e \right]^{\frac{1}{2}}
\tag{17}
$$

Proceedings of the XXXVIII Iberian Latin-American Congress on Computational Methods in Engineering
P.O. Faria, R.H. Lopez, L.F.F. Miguel, W.J.S. Gomes, M. Noronha (Editores), ABMEC, Florianópolis, SC, Brazil, November 5-8, 2017.

Nevertheless, an analytical solution is not available for most problems. Consequently, finding out a strategy to estimate the error is important. By means of the recovered stresses, this error can be estimated. Therefore, the estimated error considering the energy norm is defined in each element as

$$\left\| e^* \right\|_{\Omega_e} = \left[\int_{\Omega_e} \left(\boldsymbol{\sigma}^* - \hat{\boldsymbol{\sigma}} \right)^T \mathbf{D}^{-1} \left(\boldsymbol{\sigma}^* - \hat{\boldsymbol{\sigma}} \right) d\Omega_e \right]^{\frac{1}{2}} \tag{18}$$

The accuracy of the estimated error (recovered stresses) can be evaluated by a ratio between equations (17) and (18). This ratio is called the effectivity index and can be written in each element as

$$\Theta_{\Omega_e} = \frac{\left\| e^* \right\|_{\Omega_e}}{\left\| e \right\|_{\Omega_e}} \tag{19}$$

Obviously, the closer to the unity the effectivity index is, the more accurate the estimated error is.

All three equations above (17, 18 and 19) were defined for one element and therefore are local measures. Global measures can be computed by gathering the contributions of each element of the mesh as follows:

$$\left\| e \right\| = \left(\sum_{K=1}^{m} \left\| e \right\|_{\Omega_e, K}^2 \right)^{0.5} \tag{20}$$

$$\left\| e^* \right\| = \left(\sum_{K=1}^{m} \left\| e^* \right\|_{\Omega_e, K}^2 \right)^{0.5} \tag{21}$$

$$\Theta = \frac{\left\| e^* \right\|}{\left\| e \right\|} \tag{22}$$

where the index K denotes the element and m is the total number of elements.

4 NUMERICAL RESULTS AND DISCUSSIONS

In this section, the performance of the error estimator described in Section 3 is evaluated considering two distinct plane analysis. The first problem, detailed in Section 4.1, is a cantilever beam for which polynomial functions are employed as enrichment. The second problem, discussed in Section 4.2, is an edge crack panel for which branch and Heaviside functions are used as enrichment. The behavior of the error estimator is assessed by means of some important features for error analysis, such as: rates of convergence and effectivity indexes. Furthermore, GFEM/XFEM and SGFEM solutions are considered aiming to evaluate the robustness of the error estimator.

4.1 Cantilever beam

This problem is used to assess the accuracy of the error estimator in view of polynomial enrichments. The beam main features are represented in Figure 5. The parabolic loading on the free end is given by $q = 1.5\text{-}6y^2$. The Dirichlet boundary conditions are imposed through penalization. The Young's Modulus is taken as 100 and a Poisson's ratio value of 0.30 is adopted. In addition, plane stress conditions are assumed. The exact solution of this problem is indicated in the relations below:

$$\begin{aligned} \sigma_{xx} &= \frac{3Fxy}{2b^3} \\ \sigma_{yy} &= 0 \\ \tau_{xy} &= \frac{3F}{4b^3}\left(b^2 - y^2\right) \end{aligned} \tag{23}$$

where b corresponds to half of the height beam and $F = \int_{-b}^{b} q(y)\,dy$.

The whole set of nodes are enriched by polynomial functions. As the SGFEM already uses the linear interpolant function (see eq. (7)) for modifying the enrichment function only polynomial functions of higher order can be adopted for enrichment. In this work, only second degree shifted polynomials are explored, as follows:

$$\begin{aligned} L_x &= \frac{\left(x - x_\alpha\right)^2}{h_\alpha^2} \\ L_y &= \frac{\left(y - y_\alpha\right)^2}{h_\alpha^2} \end{aligned} \tag{24}$$

where x and y are global coordinates, x_α and y_α are nodal coordinates and h_α is a scaling factor given by the diameter of the largest element sharing node α.

In order to verify the rate of convergence, four structured meshes composed by bilinear quadrilateral elements are used. These meshes present the following grid sizes: 2 x 5, 4 x 10, 8 x 20 and 16 x 40.

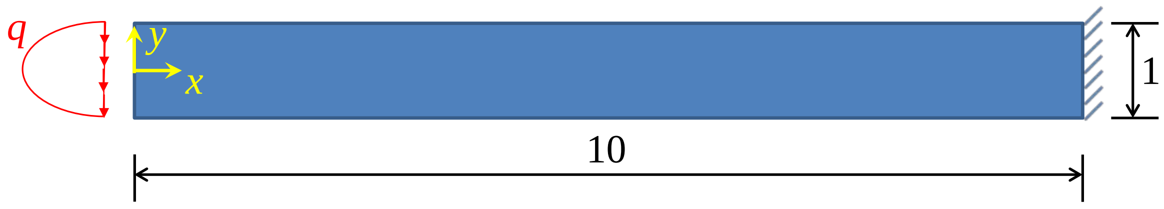

Figure 5. Cantilever beam.

Figure 6 compares the estimated and reference error in energy norm with the number of the degrees of freedom. The reference error is computed using the exact solution. As can be seen, the convergence indicated by the error estimator (on the right side) is very similar to that obtained considering the exact solution. A slightly discordance of this behavior can be noted in the first part of the curve, however, this is expected since the two first meshes are coarse.

In addition, it is remarkable in the same Figure 6 that the SGFEM is more accurate than the GFEM, despite both methods present a convergence rate close to the optimal convergence value (1.00). It is worth mentioning that such conclusion can be observed considering the exact or estimated error, indicating the efficiency of the error estimator.

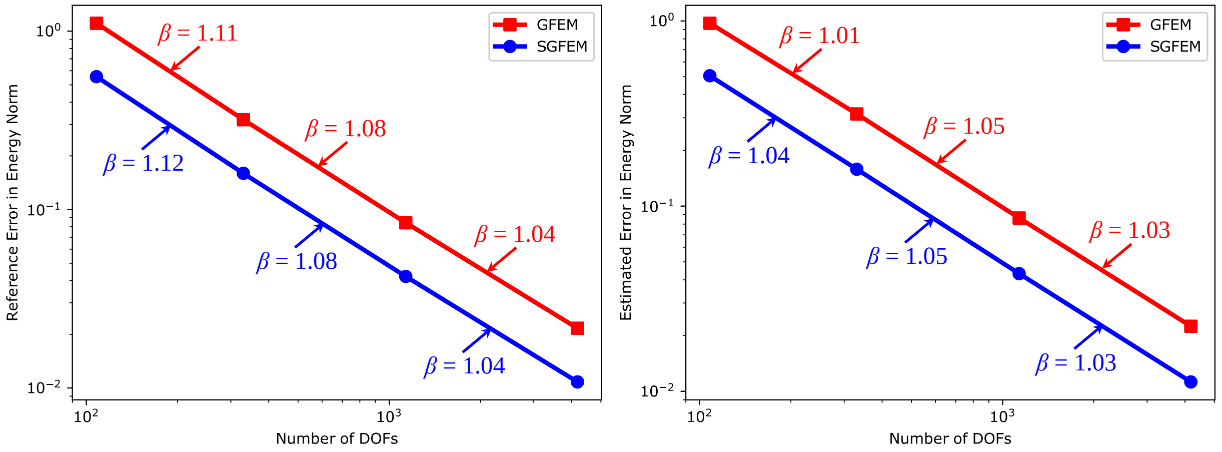

Figure 6. GFEM and SGFEM convergence calculated considering the reference (exact) error and the estimated error. The polynomial functions indicated in Eq. (24) are used as enrichment. In the figure, β denotes the convergence rate.

Figure 7 presents the effectivity indexes of the error estimator computed using the GFEM and the SGFEM. Undoubtedly, the error estimator shows a satisfactory performance for both methods as the indexes values are very close to unity. In general, the indexes computed with the GFEM and the SGFEM are very similar, but the SGFEM yields recovered stresses more accurate already for the coarsest mesh.

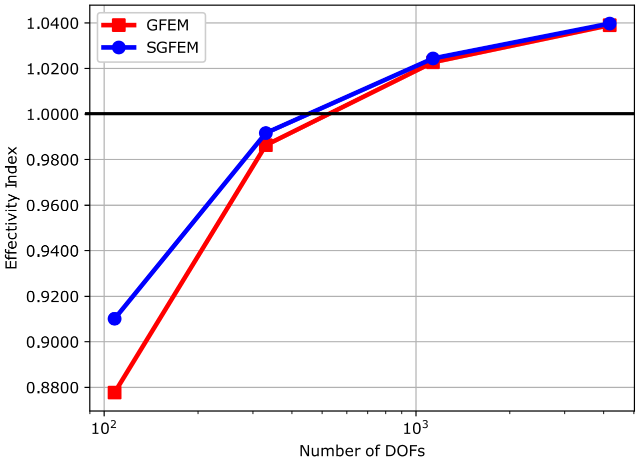

Figure 7. GFEM and SGFEM effectivity index. The polynomial functions indicated in Eq. (24) are used as enrichment.

Figures 8 and 9 depict the von Mises stress and the local error distribution for the 4 x 10 mesh. GFEM results are shown in Figure 8, whereas SGFEM results are indicated in Figure 9. It is clearly shown that the SGFEM is more accurate than the GFEM. As expected, this feature can be observed from the estimated error, despite the estimator presenting some inaccuracy where the boundary conditions are applied.

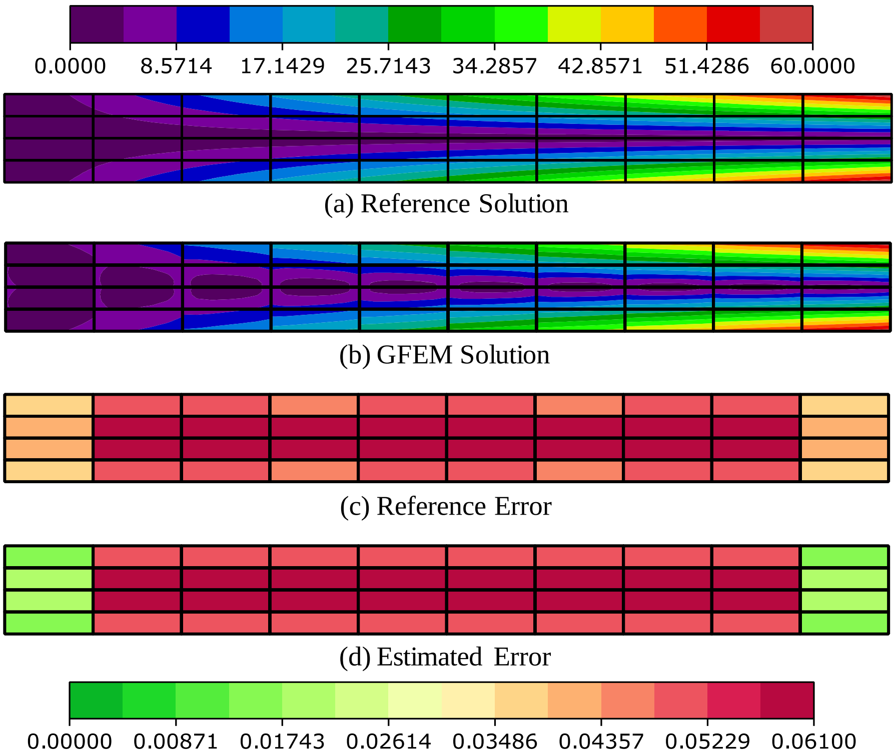

Figure 8. von Mises stresses calculated via exact and GFEM solutions (on the top) and local error (reference and estimated) distributions (on the bottom) for the 4 x 10 mesh.

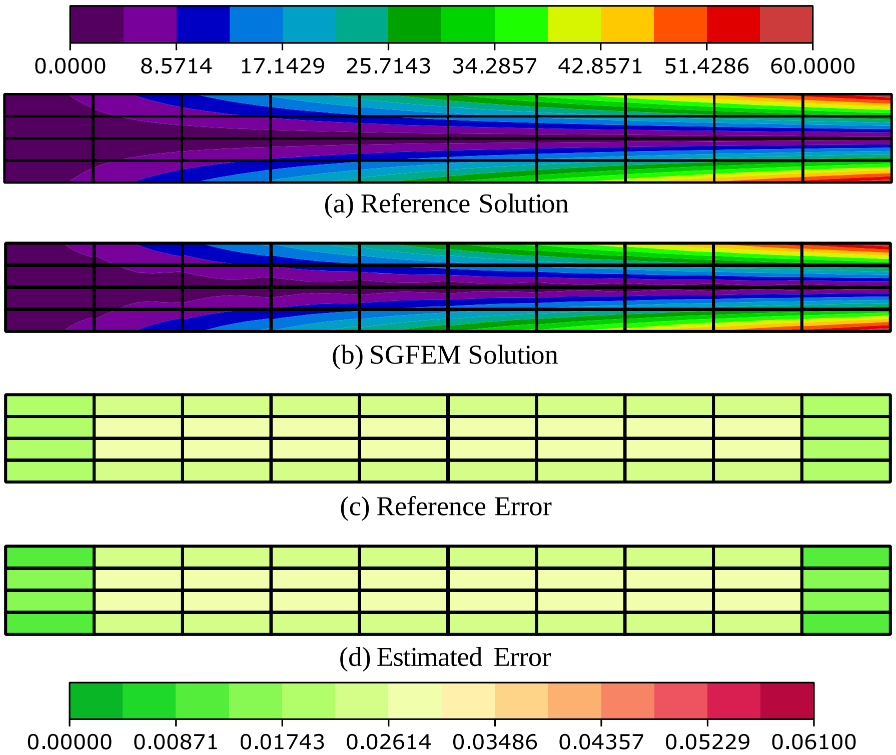

Figure 9. von Mises stresses calculated via exact and GFEM solutions (on the top) and local error (reference and estimated) distributions (on the bottom) for the 4 x 10 mesh.

4.2 Edge-crack panel

The two-dimensional linear elastic fracture problem shown in Figure 10 is considered. This problem is also analyzed in Gupta el al. (2013), however focusing on different measures of interest. The exact solution of this problem is provided by the first term of Mode I asymptotic expansions written as follows:

$$\begin{aligned}
\sigma_{xx} &= \frac{1}{4\sqrt{r}}\left(3\cos\frac{\theta}{2}+\cos\frac{5\theta}{2}\right)\\
\sigma_{yy} &= \frac{1}{4\sqrt{r}}\left(5\cos\frac{\theta}{2}-\cos\frac{5\theta}{2}\right)\\
\tau_{xy} &= \frac{1}{4\sqrt{r}}\left(\sin\frac{5\theta}{2}-\sin\frac{\theta}{2}\right)
\end{aligned} \tag{25}$$

Expressions (25) provide also Neumann boundary conditions.

The Young's Modulus is taken as a unity and a Poisson's ratio value of 0.30 is adopted. Moreover, plane strain conditions are assumed.

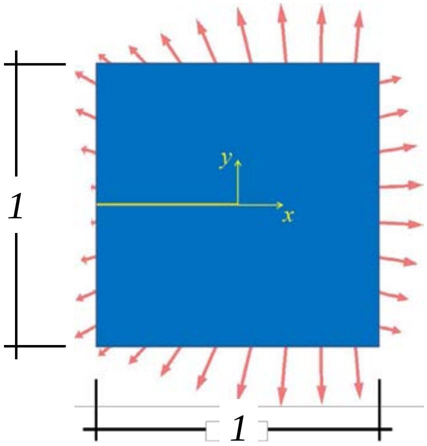

Figure 10. Two-dimensional edge-crack panel

In this example, OD branch functions are applied to the nodes belonging to a square region (side = 0.125) centralized at the crack tip. Linear Heaviside functions are employed in the crack line segment outside that region. Moreover, the nodes in the lines immediately above and below the crack line are also enriched.

Four uniform and structured meshes composed by bilinear quadrilateral elements are used to analyze the convergence of GFEM and SGFEM approximations. These four meshes present the following grid sizes: 10 x 10, 20 x 20, 40 x40 and 80 x 80. The 20 x 20 mesh with its enriched nodes is depicted in Figure 11.

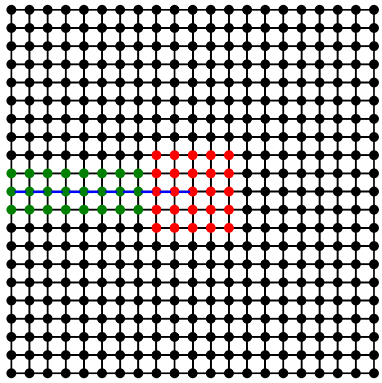

Figure 11. Illustration of the square enrichment zone and the additional enriched nodes in a 20 x 20 mesh. The red nodes are enriched with branch functions and the green nodes are enriched with linear Heaviside functions.

Figure 12 compares the estimated and reference error in energy norm with the number of the degrees of freedom. The convergence rates obtained with SGFEM are slightly higher than that obtained with GFEM. However, on average both methods provide a convergence rate close to 0.50 (optimal convergence rate), as expected. Once again, the SGFEM is clearly more accurate than the GFEM. The main reasons for this behavior are related to the accuracy over blending elements and the conditioning of the stiffness matrix. Additional details regarding this issue can be found in Lins (2015) and Gupta et al. (2013).

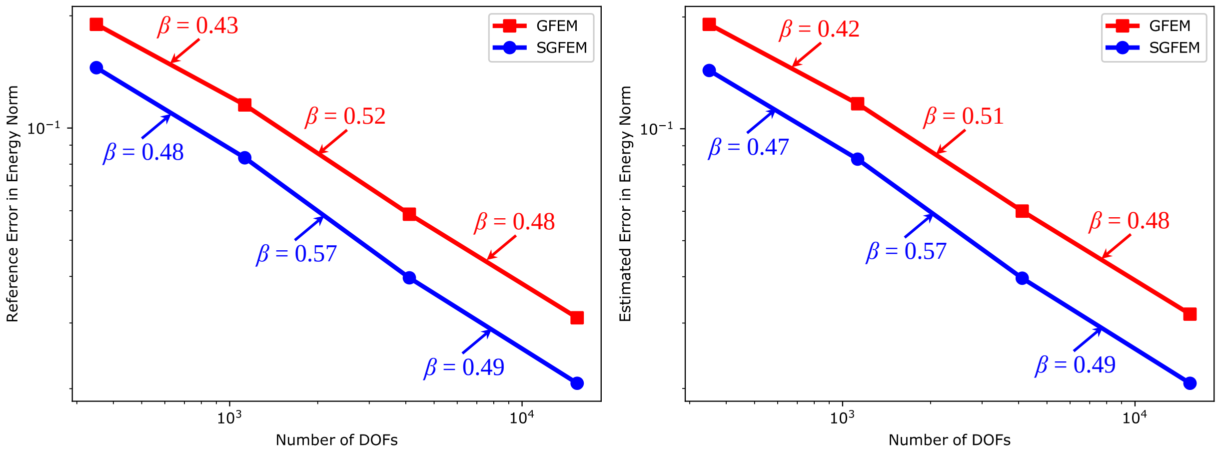

Figure 12. GFEM and SGFEM convergence calculated considering the reference (exact) error and the estimated error. Branch and linear Heaviside functions are used as enrichment. In the figure, β denotes the convergence rate.

Figure 13 shows the effectivity indexes of the error estimator computed using the GFEM and the SGFEM. For both methods, the performance of the estimator is remarkable, in particular when the SGFEM is chosen. All the indexes values are very close to unity including the coarser meshes. This result attests the accuracy of the recovered stresses obtained using the estimator for different enrichment types.

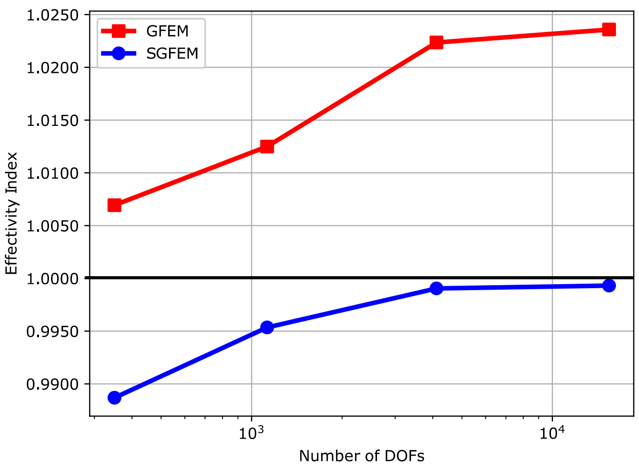

Figure 13. GFEM and SGFEM effectivity index. Branch and linear Heaviside functions are uses as enrichment.

Figure 14 illustrates the local error distribution obtained with a 20 x 20 mesh when considering OD branch and linear Heaviside enrichments. It is noticeable that the GFEM shows the highest error values in the elements containing the crack tip, whereas in the SGFEM in these same elements are found to have the smallest errors. In other words, the SGFEM is approximately two times more accurate than the GFEM (as can be seen through the labels). Furthermore, the estimated error distribution is very similar to the one obtained with the reference error. Therefore, the efficacy of the SGFEM can be visualized by means of the estimator even in problems without analytical solutions.

Figure 15 depicts the von Mises stress provided by GFEM and SGFEM for the 20 x 20 mesh using OD branch and linear Heaviside enrichments. The respective recovered stresses are shown in the same figure. Once again, it can be observed that the accuracy obtained from the SGFEM is higher than the one obtained with the GFEM in the square enriched region. As expected, the recovered stresses are very close to the exact solution in both methods. This fact explains the accuracy of the estimated error illustrated in Figure 14.

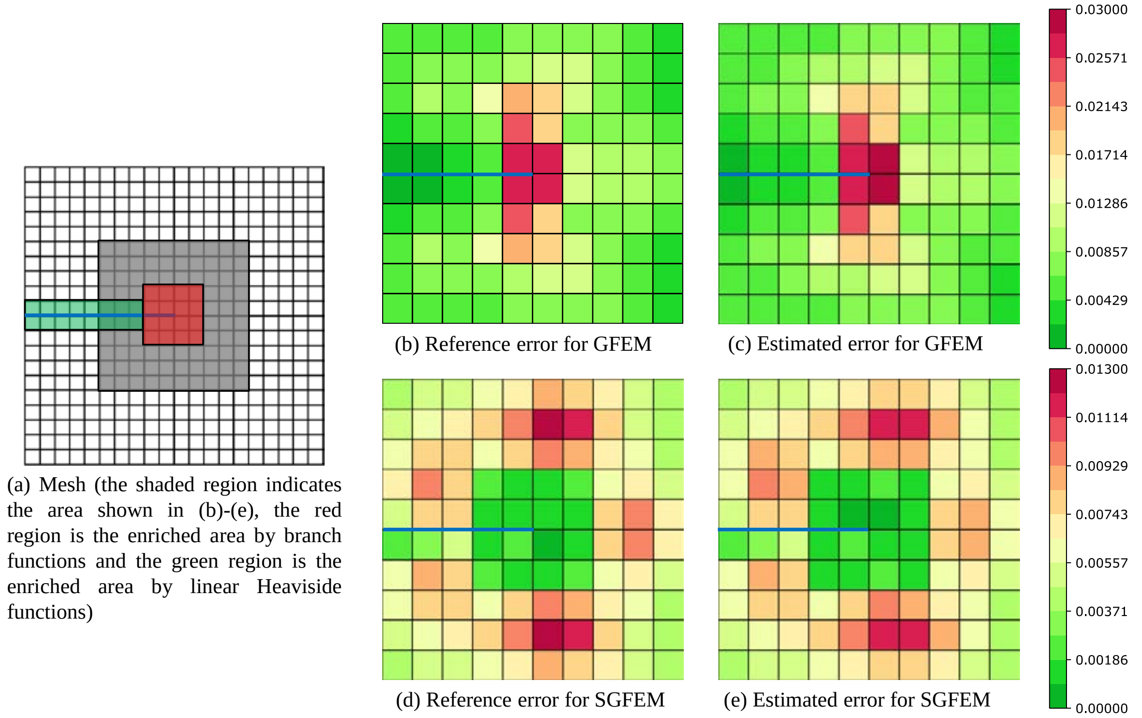

(a) Mesh (the shaded region indicates the area shown in (b)-(e), the red region is the enriched area by branch functions and the green region is the enriched area by linear Heaviside functions)

(b) Reference error for GFEM

(c) Estimated error for GFEM

(d) Reference error for SGFEM

(e) Estimated error for SGFEM

Figure 14. Local error distributions for the 20 x 20 mesh considering OD branch and linear Heaviside functions as enrichment.

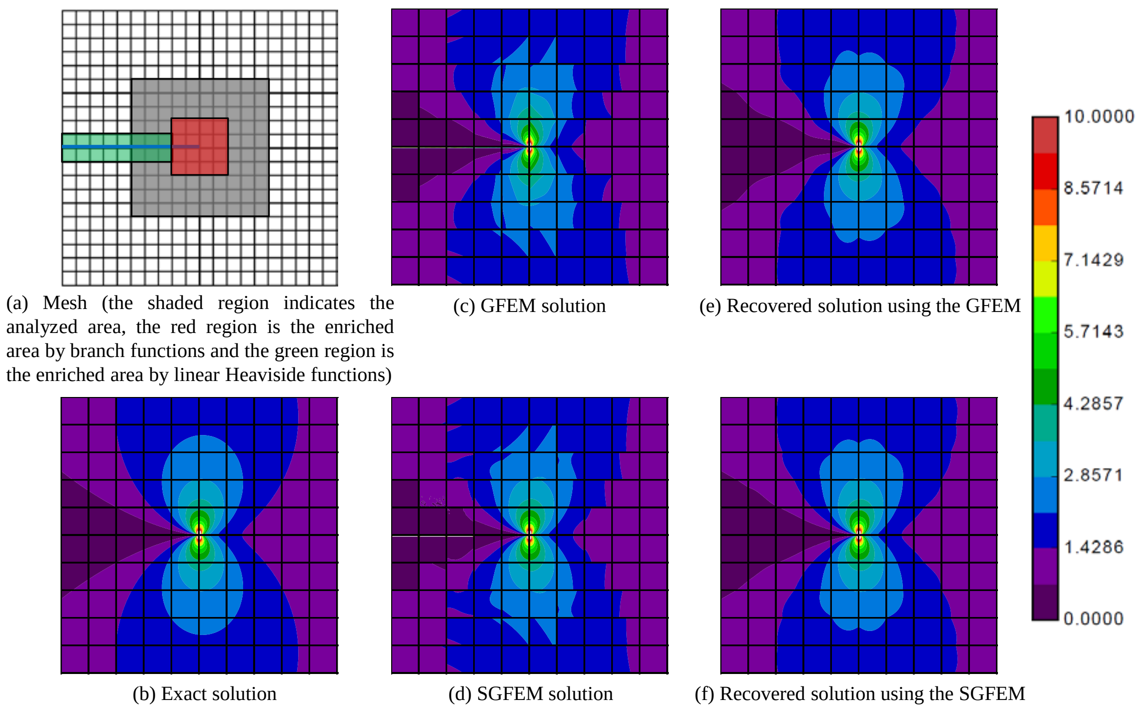

(a) Mesh (the shaded region indicates the analyzed area, the red region is the enriched area by branch functions and the green region is the enriched area by linear Heaviside functions)

(c) GFEM solution

(e) Recovered solution using the GFEM

(b) Exact solution

(d) SGFEM solution

(f) Recovered solution using the SGFEM

Figure 15. von Mises stress calculated by the GFEM and by the SGFEM and their respective recovered stresses computed by the error estimator.

5 CONCLUDING REMARKS

This paper aimed to provide a contribution to the study of the a posteriori error estimators, based on gradient recovery when applied to the GFEM/XFEM and its modified version called SGFEM. The proposed estimator combines two techniques for computing the smooth part of the recovered stress field: the SPR and the Singular Value Decomposition (SVD). Moreover, the proposed approach provided by the SVD technique can be considered more straightforward than the original SPR, since it does not require any functional. In addition the computational cost is low since the procedure involves only local (cloud) computations.

In order to fulfil this purpose, it was proposed an error estimator based on the splitting concept of the recovered stress field presented in Ródenas et al. (2008). This estimator was tested in two numerical examples involving different enrichment types, for both the standard GFEM and the SGFEM.

As a general conclusion, it can be affirmed that the error estimator hereby developed can provide accurate results for the GFEM and the SGFEM. This feature supports that the estimator can be used to verify the efficacy of the SGFEM even in problems without analytical solutions.

Regarding the comparison between GFEM and SGFEM, the set of results hereby presented corroborate to conclusions cited in Babuška and Banerjee (2012) and Gupta et al. (2013).

The performance of the error estimator was noteworthy using different enrichment types demonstrating its robustness. In particular, the confrontation of results considering polynomial enrichments in 2D domain is to the knowledge of the authors a novelty in itself.

Finally, the accuracy of the recovered stresses indicates that they can be used to replace the GFEM and also the SGFEM solutions. Furthermore, the accuracy the local estimated errors enables the development of adaptive algorithms for GFEM.

ACKNOWLEDGEMENTS

The University of São Paulo affiliated authors would like to gratefully acknowledge National Counsel of Technological and Scientific Development (CNPq) and Coordination for the Improvement of Higher Education Personnel (CAPES) for the financial support for this research project.

C.A. Duarte gratefully acknowledges the partial support from the U.S. Air Force Office of Scientific Research under contract number FA9550-12-1-0379.

REFERENCES

Babuška, I., & Banerjee, U., 2012. Stable generalized finite element method (SGFEM). *Computer Methods in Applied Mechanics and Engineering*, 201-204:91-111.

Belytschko, T., & Black, T., 1999. Elastic crack growth in finite elements with minimal remeshing. *International Journal for Numerical Methods and Engineering*, 45:601-620.

Bordas, S., Duflot, M., & Le, P., 2008. A simple error estimated for extended finite elements. *Communications in Numerical Methods in Engineering*, 24:961-971.

Duarte, C.A., Babuška, I., & Oden, J. T., 2000. Generalized finite element methods for three-dimensional structural mechanics problems. *Computer and Structures*, 77:215-232.

Fries, T-P., 2008. A corrected XFEM approximation without problems in blending elements. *International Journal for Numerical Methods and Engineering*, 75:503-532.

Gupta, V., Duarte, C.A., Babuška, I., & Banerjee, U., 2013. A stable and optimally convergent generalized FEM (SGFEM) for linear elastic fracture mechanics. *Computer Methods in Applied Mechanics and Engineering*, 266:23-39.

Ishikawa, H., Kitagawa, H., & Okamura, H.,1980. J-integral of mixed mode crack and application. In: *Proc. 3rd Int. Conf. on Mechanical Behavior of Material*, Pergamon Press, Oxford, v. 3, p. 447-455.

Jin, Y., González-Estrada, O.A., Pierard, O., & Bordas, S.P.A., 2017. Error-controlled adaptive extended finite element method for 3D linear elastic crack propagation. *Computer Methods in Applied Mechanics and Engineering*, 318:319-348.

Kim, D., Duarte, C.A., & Proença, S.P.B., 2009. Generalized finite element method with global-local enrichments for nonlinear fracture analysis. In: *Second International Symposium on Solid Mechanics*. Rio de Janeiro. Solid Mechanics in Brazil – Associação Brasileira de Engenharia e Ciências Mecânicas, 1: 317-330.

Lins, R.M., 2015. A posteriori error estimations for the generalized finite element method and modified versions. Thesis (Doctorate). São Carlos School of Engineering, University of São Paulo.

Lins, R.M., Ferreira, M.D.C, Proença, S.P.B., & Duarte, C.A., 2015. An a-posteriori error estimator for linear elastic fracture mechanics using the stable generalized/extended finite element method. *Computational Mechanics*, 56:947-965.

Moës, N., Dolbow, J., & Belytschko, T., 1999. A finite element method for crack growth without remeshing. *International Journal for Numerical Methods and Engineering*, 46:131-150.

Oden, J.T., & Duarte, C.A., 1997. Chapter: clouds, cracks and FEM's. In *Recent Developments in Computational and Applied Mechanics*, Reddy DB (ed.) International Center for Numerical Methods in Engineering, CIMNE: Barcelona, Spain, pp 302-321.

Prange, C., Loehnert, S., & Wriggers, P., 2012. Error estimation for crack simulations using the XFEM. *International Journal for Numerical Methods and Engineering*, 91:1459-1474.

Quarteroni, A., Sacco, R., & Saleri, F., 2000. *Numerical Mathematics*. Springer, New York.

Rice, J. R., 1968. A path independent integral and the approximate analysis of strain concentration by notches and cracks. *Journal of Applied Mechanics*, 35: 379-386.

Ródenas, J.J., González-Estrada, O.A., Tarancón, J.E., & Fuenmayor, F.J., 2008. A recovery type error estimator for the extended finite element method based on singular+smooth stress field splitting. *International Journal for Numerical Methods and Engineering*, 76:545-571.

Shih, C., & Asaro, R., 1988. Elastic-plastic analysis of cracks on biomaterial interfaces: part I: small scale yielding. *Journal of Applied Mechanics*, 8:537-545.

Strouboulis, T., Copps, K., & Babuška, I., 2001. The generalized finite element method. *Computer Methods in Applied Mechanics and Engineering*, 190:4081-4193.

Schweitzer, M.A., 2013, Variational mass lumping in the partition of unity method, *SIAM Journal on Scientific Computing*, 25:1073-1097.

Szabó, B., & Babuška, I., 1991. *Finite Element Analysis*. John Wiley and Sons.

Yau, J., Wang, S., & Corten, H., 1980. A mixed-mode crack analysis of isotropic solids using conservation laws of elasticity. *Journal of Applied Mechanics,* 47:335-341.

Zienkiewicz, O.C., & Zhu, J.Z., 1987. A simple error estimator and adaptive procedure for practical engineering analysis. *International Journal for Numerical Methods and Engineering*, 24:337-357.

Zienkiewicz, O.C., & Zhu, J.Z., 1992a. The superconvergent patch recovery and a posteriori error estimates. Part 1: the recovery technique. *International Journal for Numerical Methods and Engineering*, 33:1331-1364.

Zienkiewicz, O.C., & Zhu, J.Z., 1992b. The superconvergent patch recovery and a posteriori error estimates. Part 2: error estimates and adaptivity. *International Journal for Numerical Methods and Engineering*, 33:1365-1382.